Phonon signatures of multiple topological quantum phase transitions in compressed $TlBiS_2$: A combined experimental and theoretical study

V. Rajaji,[1,2] Raagya Arora,[1,2] Saurav Ch. Sarma,[3,2] B. Joseph,[4] Sebastian C. Peter,[3,2]
Umesh V. Waghmare,[5,2] and Chandrabhas Narayana[1,2,*]

[1]*Chemistry and Physics of Materials Unit, Jawaharlal Nehru Centre for Advanced Scientific Research, Jakkur P.O., Bangalore 560 064, India*
[2]*School of Advance Materials, Jawaharlal Nehru Centre for Advanced Scientific Research, Bangalore 560 064, India*
[3]*New Chemistry Unit, Jawaharlal Nehru Centre for Advanced Scientific Research, Jakkur P.O., Bangalore 560 064, India*
[4]*Elettra Sincrotrone Trieste, S.S. 14, Km 163.5 in Area Science Park, Basovizza, Trieste 34012, Italy*
[5]*Theoretical Sciences Unit, Jawaharlal Nehru Centre for Advanced Scientific Research, Bangalore 560 064, India*

(Received 7 February 2019; revised manuscript received 12 April 2019; published 21 May 2019)

We report the hydrostatic pressure induced two topological phase transitions in strong spin-orbit coupled material $TlBiS_2$ at room temperature. Frequencies of the A_{1g} and E_g phonons are observed to increase monotonically up to ∼4.0 GPa, but with a clear slope change in A_{1g} mode at ∼1.8 GPa. Interestingly, there are two clear anomalies noticed in phonon linewidths of E_g mode at pressures ∼0.5 and ∼1.8 GPa. Such anomalies are evidence of isostructural electronic transitions associated with unusual electron-phonon coupling. The high-pressure synchrotron powder diffraction and Raman show a first-order phase transition above 4 GPa. First-principles density functional theory-based calculations of electronic band structure, topological invariant $\mathbb{Z}_2$ and mirror Chern number n_M reveal that the phonon anomalies at ∼0.5 and ∼1.8 GPa are linked to the band inversions at Γ and F points of the Brillouin zone respectively. The first band inversion at Γ point at ∼0.5 GPa changes the $\mathbb{Z}_2$ from 0 to 1 leading to the transition of $TlBiS_2$ system into a topological insulator. The second band inversion at F point at ∼1.8 GPa results in $n_M = 2$, revealing a transition to a topological crystalline insulating state. Therefore the applied pressure systematically tunes the electronic states of $TlBiS_2$ from a normal semiconductor to a topological insulator and finally into a topological crystalline insulator at two distinct pressures of ∼0.5 and ∼1.8 GPa respectively, before undergoing a structural phase transition at ∼4 GPa.

DOI: 10.1103/PhysRevB.99.184109

I. INTRODUCTION

Topological insulators (TIs) are a new kind of electronic state of matter which has spin polarized conducting states at their surface and insulating states in its bulk. The existence of time-reversal symmetry gives the protection to the topological surface states against nonmagnetic impurities or defects [1]. TI has potential applications in spintronics and quantum computation devices. Apart from these, TI also offers the useful platform for realizing quantum particles like Majorana fermions in the condensed matter system [1]. At first, theoretical prediction of TI has been made in HgTe/CdTe quantum wells [two-dimensional (2D)] [2] and then subsequently experimentally observed [3]. Soon after this discovery, TI in 3D bulk materials [various strong spin-orbit coupling (SOC) systems] has been theoretically predicted [4] and confirmed using angle-resolved photoemission spectroscopy (ARPES) at ambient conditions [5–7]. Interestingly, some narrow band gap materials (at ambient conditions) with strong SOC can be tuned to a TI by external strain [8,9]. The nonadiabatic process in which the normal bulk insulator can be tuned into a TI is called the topological quantum phase transition (TQPT). During the TQPT, the topological invariant quantity $\mathbb{Z}_2$ characterizes the changes in the electronic state of the system ($\mathbb{Z}_2 = 0$ trivial insulator and $\mathbb{Z}_2 = 1$ nontrivial insulator) [1,10]. The $\mathbb{Z}_2$ is the product of parities at the time-reversal invariant momenta (TRIM) point of the Brillouin zone (BZ) of the system. In general, the strain can be applied to the system either by chemical (doping or substitution) or physical methods (lattice compression). Compared to the chemical route which induces chemical disorder (inhomogeneities) in the system, a physical route is cleaner (no atomic scale chemical inhomogeneities) and is thus more appropriate.

Another interesting class of materials are called as topological crystalline insulators (TCI) [11,12], where the gapless surface states are protected by mirror symmetry. These materials are different from TI in which the time-reversal symmetry protects the surface states and hence the protection of surface states for TCI perseveres even when time-reversal symmetry is broken. The presence of mirror symmetry in the crystal structure of a material results in the presence of planes in the BZ that are mirror symmetric. Therefore mirror symmetry protected Dirac cones arise in the surface electronic structure. TCIs are characterized by a nonzero mirror Chern number. The individual Chern numbers C_{+i} and C_{-i} are defined on a mirror-invariant plane. The mirror Chern number [11] defined as $n_M = (C_{+i} - C_{-i})/2$ can be used as a topological invariant for TCI. A TCI supports an even number of Dirac cones and band inversions in sharp contrast to a TI characterized by odd number of band inversions. The first TCI state experimental [13] observation was made in SnTe, which were earlier theoretically [14] predicted.

*Corresponding author: cbhas@jncasr.ac.in

The narrow band gap tetradymite semiconductors Bi_2Se_3 (band gap $E_g = 0.30$ eV), Bi_2Te_3 ($E_g = 0.12$ eV), and Sb_2Te_3 ($E_g = 0.28$ eV) crystallize in rhombohedral structure (space group SG: $R\bar{3}m$) and are 3D TI at ambient conditions with surface states consisting of a single Dirac cone at the Γ point of the BZ [4–7]. In the tetradymite semiconductors family, the Sb_2Se_3 is having the larger band gap ($E_g \sim 1$ eV) and lesser SOC strength than remaining members (Bi_2Se_3, Bi_2Te_3, and Sb_2Te_3). There are no topologically non-trivial states present at ambient conditions in Sb_2Se_3. It is well known that the thermodynamic parameter pressure P can tune the strength of the SOC and also the band gap. Interestingly, hydrostatic pressure induced band inversion with parity change at Γ point in the Sb_2Se_3 compound has been theoretically predicted [15] and then subsequently phonon anomalies are noticed at ∼2.5 GPa [16]. Similarly, thallium based III-V-VI_2 ternary chalcogenides $TlBiSe_2$ ($E_g = 0.28$ eV) and $TlBiTe_2$ ($E_g = 0.11$ eV) crystallize in rhombohedral structure (SG: $R\bar{3}m$) and are 3D TI at ambient conditions [17]. In this family, $TlBiS_2$ ($E_g = 0.42$ eV) is having relatively higher band gap and lesser SOC than $TlBiSe_2$ and $TlBiTe_2$ compounds. Under the application of external strain, the TQPT is theoretically predicted in the $TlBiS_2$ system [18]. The above two examples (tetradymite semiconductors and thallium based III-V-VI_2 ternary chalcogenides) illustrate the interplay between the crystal symmetry, band gap, and SOC. In other words, when the compound of 3D TI family shares the same crystal and electronic structure, but lacks the band gap and SOC, and then pressure can serve as an ideal external tool to induce the band inversion in it.

Thallium based III-V-VI_2 ternary chalcogenide $TlBiS_2$ is the narrow band gap semiconducting material and has significant interest on the aspect of thermoelectric and topological properties under different conditions [18]. Even though $TlBiS_2$ share the same crystal structure (SG: $R\bar{3}m$) as tetradymite compounds (Bi_2Se_3, Bi_2Te_3, and Sb_2Te_3), there is a considerable difference exists between them. The tetradymite semiconductors consist of quintuple layers stacking along the c axis, and each quintuple layers are separated by weak Van der Waals type interactions and therefore it is a quasi-2D nature. In $TlBiS_2$, each Tl (or Bi) layer is sandwiched between the two S layers. However, strong coupling exists between the two layers and makes it intrinsically 3D natures [18,19]. Recently, it is observed that the substitution of Se ($x \sim 0.5$) at S site [$TlBi(S_{1-x}Se_x)_2$], leading to the formation of a single Dirac cone at the Γ point [20]. Here, the substituted Se (i) increases the effective SOC strength of $TlBiS_2$ compound without changing the crystal structure, and (ii) decreases the band gap. Consequently, nontrivial topological phase transition ($\mathbb{Z}_2 = 1$) is observed in [$TlBi(S_{1-x}Se_x)_2$] at ambient pressure. This interesting chemical approach strongly stimulated us to perform the high-pressure studies on $TlBiS_2$. Because the substitution of Se is analogous to the externally applied pressure which can also possibly tune the effective hybridization, the relative strength of the SOC, band gap, and topological invariant $\mathbb{Z}_2$. To support our intuition further, recently, first-principles theoretical calculations predicted the topologically nontrivial phases in rhombohedral phase (SG: $R\bar{3}m$) of $TlBiS_2$ under different strain effects (uniaxial, biaxial and hydrostatic strains) [18]. However, to the best of our knowledge, to date, there is no strain dependent experimental work available on the $TlBiS_2$ compound in the literature. Also, we would like to mention here that the hydrostatic pressure is effective, well controlled and experimentally easily accessible strain using the diamond anvil cells (DAC).

To probe the band inversion, ARPES can be utilized which directly provide signatures in the electronic band structure. However, ARPES measurements under high-pressure conditions using DAC are experimentally not feasible at present. But, the techniques like Raman scattering, synchrotron x-ray diffraction (XRD), and transport measurements can provide the indirect experimental signatures of topological transitions [9,16,21–23]. When theoretical calculations applied together with such indirect experimental techniques, it is possible to shed light on the pressure induced topological transitions [16,21,24]. In the present work, we have extensively used the Raman spectroscopy for probing the indirect of signatures of topological transitions in $TlBiS_2$. During the topological transitions (TI and TCI), band inversions with parity changes are expected. As a consequence of such band inversions, electron-phonon coupling changes are noticed in several systems [16,21,24,25]. Raman linewidth is one of the best indicators for the electron-phonon coupling changes [16,21,24–26]. Recently, the first-principles theoretical calculations established the connection between the Raman linewidth and topological (band inversion) transition [27]. In specific, it is shown that the square of the energy-resolved electron-phonon matrix elements is directly related to Raman linewidth [27]. Therefore, signatures of topological transitions (band inversions) will be strongly replicated in electron-phonon coupling changes (i.e., Raman linewidth) and thus provide a good indicator for detecting the indirect signatures of topological transitions. Particularly, for the centrosymmetric crystal, the long-wavelength optical phonon ($q = 0$) can effectively couples to electrons either through anticommutation or commutation with an electronic parity operator [27]. Therefore topological invariant changes (band inversions) are reflected in Raman linewidth. Based on the above mentioned principle, the topological transitions are experimentally evidenced through phonon linewidth anomalies in some specific systems such as BiTeI, Sb_2Se_3, 1T-$TiTe_2$, 1T-$TiSe_2$, and black phosphorous [16,21,22,24,25]. In fact, these compounds were theoretically predicted as the pressure induced TIs using the band structure calculations [8,15,28–30]. So, the established theoretical calculations [27] and experimental measurements on various systems [16,21,22,24,25] clearly illustrates the importance of using Raman scattering for detecting the topological transitions. It is also noteworthy that the Shubnikov–de Haas oscillations measurements [31] on BiTeI single crystal signatures the TQPT through the Fermi surface shape changes under pressure, which ascertain the earlier claim of topological transitions using Raman linewidth anomalies on this system. Hence, it will be interesting to explore the possibility of hydrostatic pressure tuned topological phase transitions in $TlBiS_2$ using Raman scattering complemented with the synchrotron XRD measurements and theoretical first-principles calculations.

In this paper, we have investigated the pressure dependent structural and vibrational properties of the rhombohedral phase of $TlBiS_2$ compound using *in situ* synchrotron XRD

and Raman scattering measurements respectively. Combined Raman and synchrotron XRD results indicate that the rhombohedral phase shows the structural stability up to ∼4.0 GPa and beyond which the first-order structural phase transition takes place. Further, two isostructural electronic transitions are observed from phonon (E_g and A_{1g}) anomalies at ∼0.5 and ∼1.80 GPa and corroborated with our first-principles theoretical calculations to TQPT ($\mathbb{Z}_2 = 1$) and TCI ($n_M = 2$) transitions, respectively. Finally, the significance of the obtained results is discussed in connection with other known pressure induced topological materials.

II. EXPERIMENTAL DETAILS

The pure phase of $TlBiS_2$ single crystal was synthesized by Bridgeman method and details are given in Ref. [32].

Raman spectra were recorded using LabRam HR evolution (Horiba) micro Raman spectrometer in the backscattering geometry (180°). This commercial Raman spectrometer equipped with a solid-state four level laser (Nd:YAG, wavelength $\lambda = 532$ nm), 800 mm focal length monochromator, and Peltier cooled CCD detector. The resolution of the spectrometer is about $\sim 0.8\,cm^{-1}$ for the grating of 1800 groves per mm and 200 μm entrance slit width. The *in situ* high-pressure Raman scattering measurements were carried out using a typical Mao Bell DAC with the culet size of 400 μm. The stainless steel (T301) was used as a gasket material, and it was preindented to the thickness of about 60 μm. The pressure was determined by the ruby fluorescence method [33]. The methanol:ethanol (4:1) mixture was used as the pressure transmitting medium (PTM) which maintains the hydrostatic condition up to 10.5 GPa [34]. The typical accumulation time of each spectrum was about 25 minutes. The laser power was kept at a lower value (<0.5 mW) which prevents the sample from laser induced damage and oxidation.

The *in situ* high-pressure XRD measurements were performed using Mao Bell DAC at Xpress beamline of the Elettra synchrotron radiation facility, Trieste, Italy. The wavelength (λ) of the synchrotron radiation used is ∼0.50070 Å. The MAR-345 imaging plate detector is used for the present experiment. Initially, the sample to detector distance was calibrated with a LaB_6 sample and found to be ∼271.38 mm. The gasket preparation, pressure calibration and PTM used are the same as above mentioned in the case of high-pressure Raman scattering experiments. Typical accumulation time for each collected synchrotron XRD pattern is 10 minutes. The collected two-dimensional (2D) diffraction image patterns were converted to one-dimensional (1D) patterns (intensity versus 2θ) using the fit2D software [35]. The Le Bail method fitting of the powder XRD patterns was performed using the FULLPROF software [36].

III. COMPUTATIONAL METHODS

Our first-principles theoretical calculations are based on density functional theory (DFT) employing the QUANTUM ESPRESSO (QE) code [37]. We used a generalized gradient approximation (GGA) [38] to the exchange-correlation energy functional as parametrized by Perdew, Burke, and Ernzerhof (PBE) [39]. The projector augmented wave (PAW) potentials [40] with valence configuration $4f^{14}\ 6s^2\ 6p^1\ 5d^{10}$, $4f^{14}\ 6s^2\ 6p^3\ 5d^{10}$, and $4d^{10}\ 5s^2\ 5p^2$ were adopted for Tl, Bi, and S, respectively. Electronic wave functions and charge density were represented in plane wave basis sets truncated with cutoff energies of 55 and 550 Ry respectively. The discontinuity in occupation numbers of electronic states was smeared using a Fermi-Dirac distribution function with broadening of $k_BT = 0.003$ Ry and integrations over BZ were sampled on a uniform $6 \times 6 \times 6$ mesh of k points. In the simulation of pressure-dependent properties, we used scalar-relativistic PAW potentials to optimize the structure with respect to lattice constants and atomic coordinates. The structure was optimized to minimize the enthalpy, $H = E + PV$ at a given pressure. We used scalar relativistic potentials since minimization of stresses using fully relativistic pseudopotentials of the above form are not possible. The effect of SOC was included by taking the atomic coordinates of the structure optimized using scalar relativistic potentials as the initial structure to further minimize the forces on atoms using fully relativistic potentials. The scheme mentioned above was adopted for structure optimization where first both stresses and forces were reduced using scalar relativistic PAW potentials followed by minimization of forces using fully relativistic PAW potentials. Electronic structure calculations were performed using fully relativistic pseudopotentials [41] since for this class of materials; SOC plays a crucial role in the formation of topological states and has significant strength. We used scalar-relativistic PAW potentials in the calculation of phonons. Electronic spectrum was determined at Bloch vectors along high-symmetry lines (Γ- L- Z- F- Γ-Z) in the BZ. Lattice dynamical properties were determined using density functional linear response (called as density functional perturbation theory [42]) as implemented in the QE package [37]. To obtain phonon dispersion, dynamical matrices were obtained on a $2 \times 2 \times 2$ q points grid in the BZ. We Fourier interpolated these dynamical matrices to obtain the phonon dispersion along high symmetry lines (Γ- L-Z-F-Γ-Z) in the BZ. To determine the bulk electronic topology of $TlBiS_2$, we used Z2PACK code [43] to calculate the $\mathbb{Z}_2$ topological invariants and mirror Chern number (n_M). This code uses hybrid Wannier functions [44,45] and employs the ideas of time-reversal polarization in the determination of the $\mathbb{Z}_2$ invariants.

IV. RESULTS

A. Ambient characterization

At ambient conditions, $TlBiS_2$ adopts the rhombohedral structure with Tl^{1+}, Bi^{3+}, and S^{2-} atoms occupying 3a, 3b, and 6c Wyckoff sites, respectively. The schematic of the unit cell of $TlBiS_2$ is shown in the Fig. 1(a). In this centrosymmetric structure, both Bi and Tl site act as the inversion center. The Rietveld refinement of the ambient XRD pattern of $TlBiS_2$ is shown in the Fig. 1(b). The calculated lattice parameters are $a = 4.1083$ Å, $c = 21.8660$ Å, and $V = 319.61$ Å^3 which agrees well with the previous literature [46]. The refined atomic fractional coordinates of Tl, Bi, and S are (0,0,0.5), (0,0,0), and (0,0,0.2624), respectively. Here the only

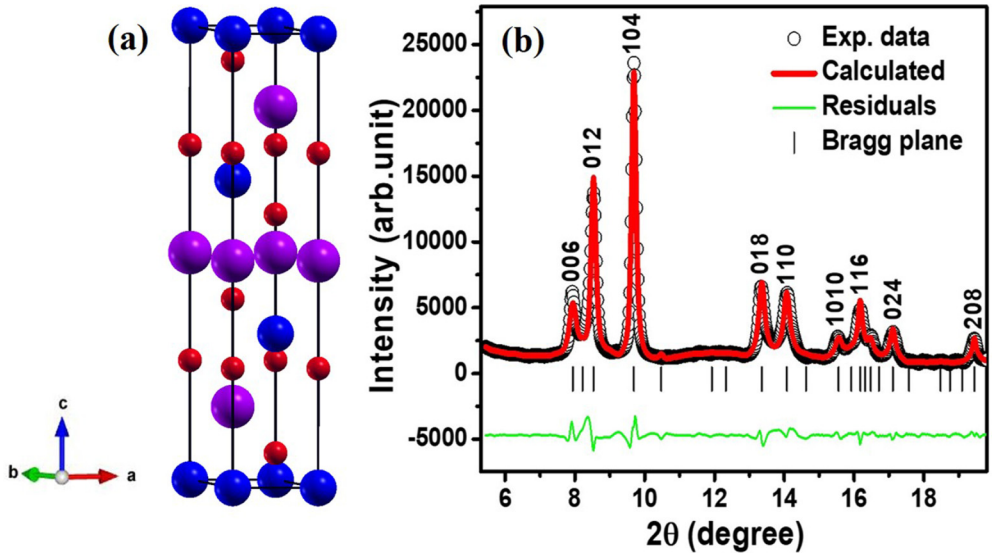

FIG. 1. (a) Unit cell of the hexagonal (supercell) phase of $TlBiS_2$ (blue, violet, and red spheres represents the Tl, Bi, and S atoms, respectively) and (b) Rietveld refinement of the XRD pattern for $TlBiS_2$ at ambient conditions ($\lambda = 0.50070$ Å).

free positional fractional coordinate is z of the S atom, and it controls the hybridizations between the two layers.

According to group theoretical analysis, the rhombohedral structure (D^5_{3d}) of $TlBiS_2$ compound has 12 zone center phonon modes:

$$\Gamma = A_{1g} + 3A_{2u} + 3E_u + E_g.$$

Here, there are two Raman active modes ($A_{1g} + E_g$) and four infrared (IR) active modes ($2A_{2u} + 2E_u$). The acoustic phonon $\Gamma_{acoustic} = A_{2u} + E_u$. The subscript g and u represent the gerade and ungerade modes, respectively. Based on our DFT based phonon mode calculations, the observed Raman mode at ~211 and ~242 cm^{-1} are assigned to E_g and A_{1g} symmetry respectively. The schematic of displacement patterns for phonon modes is shown in the Figs. 2(b)–2(d). As evident from Figs. 2(b)–2(d), the A_{1g} and E_g mode represents the out of plane (along c axis) and in-plane (along the ab plane) vibrations respectively. The comparison between the experimental and theoretical phonon frequencies are given in the Table I. Also, we have calculated the phonon dispersion of $TlBiS_2$ at ambient conditions with and without SOC (see Fig. S1 in Ref. [32]) and the results are discussed in Ref. [32]. Figure S1 shows the absence of negative frequencies in it indicating the structure (rhombohedral) is stable.

B. X-ray diffraction measurements under pressure

Typical XRD patterns of $TlBiS_2$ at selected pressure values up to ~6.00 GPa are shown in the Fig. 3. As evident from Fig. 3, the rhombohedral structure of $TlBiS_2$ is stable up to ~4.00 GPa. After that, the appearance of new Bragg peaks above ~4.00 GPa indicates the structural phase transition. The

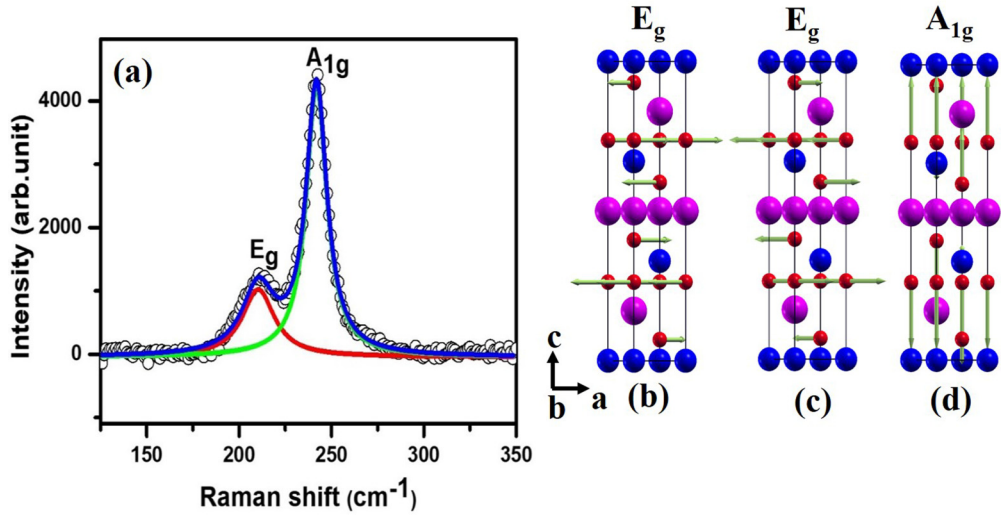

FIG. 2. (a) Experimental Raman spectrum of $TlBiS_2$ at ambient conditions, and (b) visualization of the atomic displacement patterns for the E_g and A_{1g} modes obtained from calculations. The blue, violet, and red spheres represents the Tl, Bi, and S atoms, respectively.

TABLE I. Raman mode assignment of the rhombohedral phase of $TlBiS_2$.

Raman mode	Experimental frequency (cm^{-1})	Theoretical frequency (cm^{-1})
E_g	211	200
A_{1g}	242	234

structural phase transition is fully reversible upon decreasing pressure to ambient condition (see Fig. 3). The main emphasis of the present work is only on the investigation of possible topological transition in the rhombohedral phase of $TlBiS_2$. Therefore the detailed study of pressure induced structural phase transitions in $TlBiS_2$ compound is the future interest of our group. The presence of strong texture affects the obtained XRD patterns; hence we could not do the full Rietveld refinement reliably. However, we have done the Le Bail method fitting of the obtained XRD patterns (for each pressure values), which gives the accurate unit cell parameters (a, c, and V). Figures 4(a) and 4(b) represents the Le Bail fit of the synchrotron XRD pattern at ~1.55 and 3.92 GPa, respectively [for other pressure values, please see Figs. S2(a) and S2(b) in Ref. [32]. The pressure dependence of the lattice parameters (a and c) are shown in the Fig. 5(a). The monotonic decrease in a and c are observed under pressure up to ~4.0 GPa. The pressure dependence of the unit cell parameters (a and c) are fitted by Murnaghan equation of state (EOS) [47] using EOSFIT7 software and the fit yields the linear compressibility of a axis K_a (or K_b) $= 9.25 \times 10^{-3}$ GPa^{-1} and that of c axis, $K_c = 9.58 \times 10^{-3}$ GPa^{-1}. The obtained values of linear compressibility suggesting us that lattice parameters a and c are having more or less similar compressibility (isotropic nature), which is consistent with the 3D nature of $TlBiS_2$ crystal structure. Further, the systematic decreasing trend in c/a ratio under pressure was observed [see the inset of Fig 5(a)]. Mention must be made that there is no anomaly found in lattice parameters (a and c) and c/a ratio within the experimental accuracy. The pressure dependent unit cell volume data is best fitted [see Fig. 5(b)] by Murnaghan EOS [47] which is given below:

$$P(V) = \frac{B_o}{B_o'}\left[\left(\frac{V_o}{V}\right)^{B_o'} - 1\right],$$

where V_0, B_0, and B_0' are volume at ambient pressure, isothermal bulk modulus $[-V/(dV/dP)]$, and the first-order derivative of bulk modulus, respectively. The Murnaghan EOS was used to fit the pressure region up to ~4.00 GPa and the fit yields $V_0 = 319.584$ Å^3, bulk modulus $B_0 = 37.65$ GPa and $B_0' = 5.7$. Here, the obtained value of bulk modulus ($B_0 = 37.65$ GPa) for $TlBiS_2$ is lower than tetradymite semiconductors (Bi_2Se_3 ($B_0 = 53$ GPa) [48] and Sb_2Te_3 ($B_0 = 54.7$ GPa) [49]), and hence $TlBiS_2$ is relatively softer.

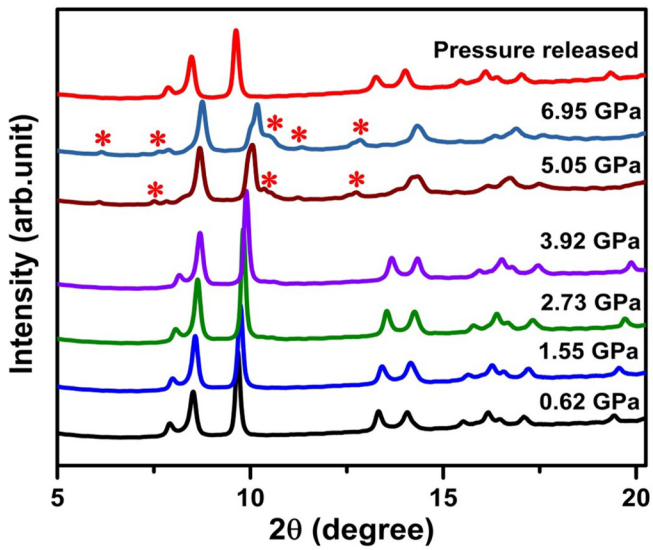

FIG. 3. Pressure dependence of the synchrotron XRD patterns ($\lambda = 0.50070$ Å) of $TlBiS_2$ at selected pressure values. The red color asterisk symbol represents the appearance of new peaks.

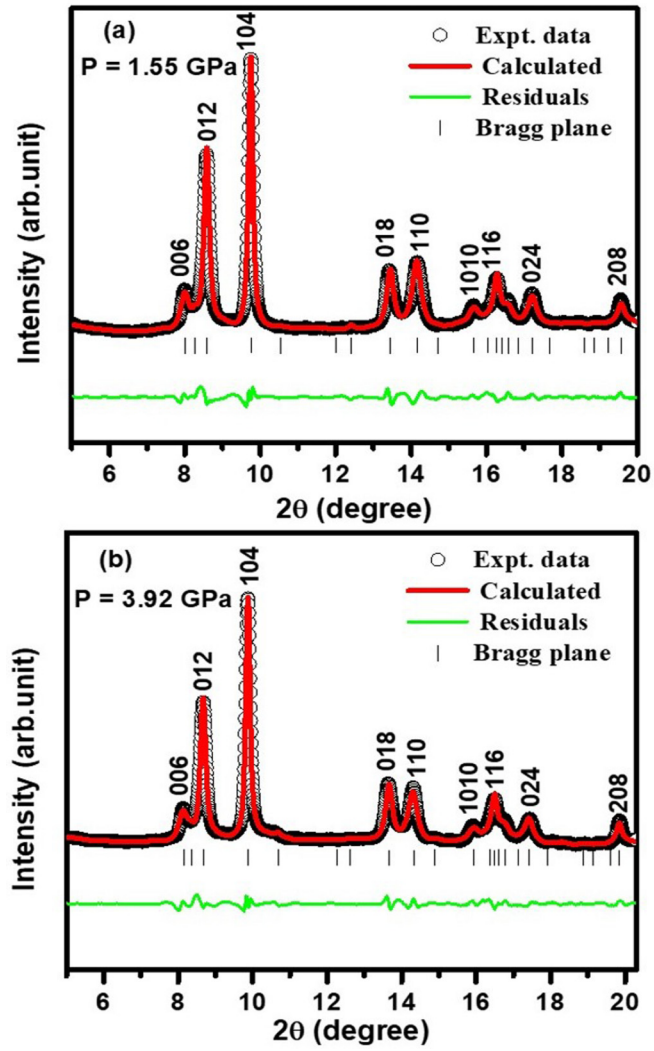

FIG. 4. Le Bail fit to the synchrotron XRD patterns ($\lambda = 0.50070$ Å) of $TlBiS_2$ at (a) 1.55 and (b) 3.92 GPa.

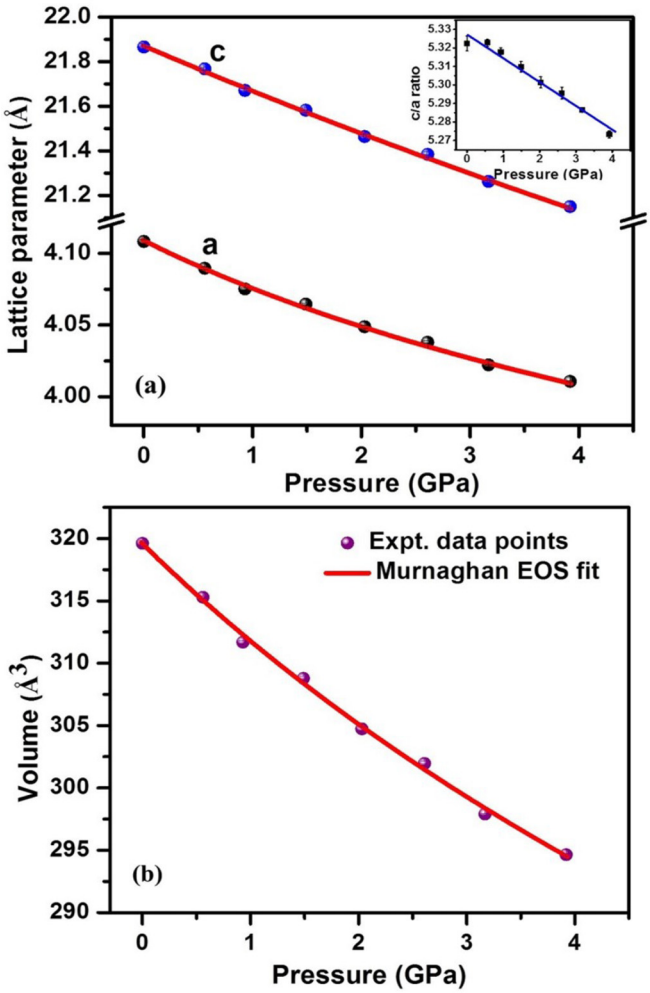

FIG. 5. (a) Pressure dependence of the lattice parameters (a and c) of $TlBiS_2$. The inset shows the P vs c/a ratio. (b). Pressure vs volume of $TlBiS_2$. The red and blue solid line represents the Murnaghan EOS fit and guide to the eye, respectively.

C. Raman scattering measurements under pressure

Raman spectroscopy is a local sensitive technique which can be extensively used for studying the structural, electronic, and topological transitions in the system [16,25,26,48]. So, to explore the lattice dynamical properties of the rhombohedral phase of $TlBiS_2$ compound, we have carried out the high-pressure Raman scattering measurements up to ∼6.0 GPa. Figure 6 represents the pressure evolution of the Raman spectrum of $TlBiS_2$ up to ∼6.0 GPa. As the pressure increases, the intensity of both modes (E_g and A_{1g}) is increased. After ∼4 GPa, the appearance of five new Raman peaks and disappearance of rhombohedral phase Raman active peaks (E_g and A_{1g}) indicates the structural phase transitions. Raman mode's frequency is the thermodynamic order parameter which is particularly sensitive to the type of the structural phase transition (whether first- or second-order) under perturbations. Hence, to get the more insight about this structural transition, we have analyzed the pressure dependent phonon mode frequencies up to ∼6.0 GPa and plotted in Fig. S3 (see Ref. [32]). The sharp discontinuity at ∼4.0 GPa in Fig. S3 confirms the first-

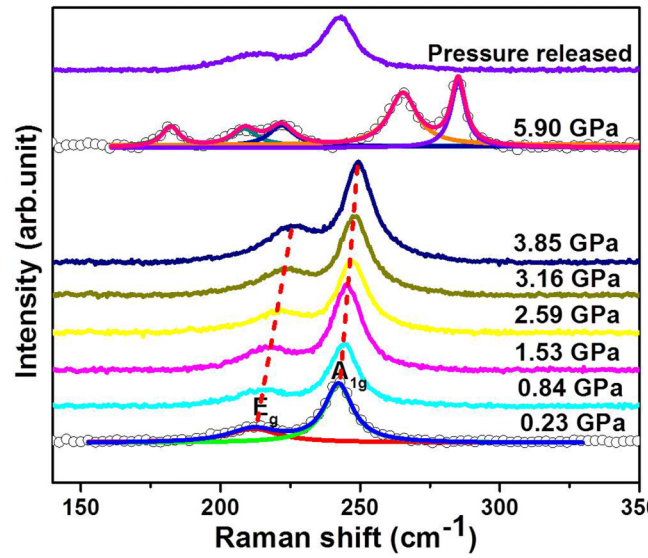

FIG. 6. Experimental Raman spectrum of $TlBiS_2$ at different selected pressures up to ∼5.9 GPa.

order structural phase transition in $TlBiS_2$ which is consistent with the XRD results. Figures 7(a)–7(d) shows the pressure dependence of the A_{1g} and E_g modes (only the rhombohedral phase) of $TlBiS_2$ single crystal. We have used instrumental error in Figs. 7(a)–7(d) and the details of the error in our experimental data analysis is commented in Ref. [32]. Generally, the systematic hardening (increasing) of phonon modes is expected under hydrostatic lattice compression. Here, the frequency of both the modes (A_{1g} and E_g) hardening up to ∼4.0 GPa, but A_{1g} mode shows the significant change in its slope at ∼1.80 GPa. The pressure-dependent behavior of the E_g phonon mode is fitted using a linear equation up to ∼4.0 GPa, whereas for A_{1g} modes, the linear equation is used for two different pressure regions (0–1.8 and 1.8–4.0 GPa). The linear fitting of the experimental (expt) data 1, is shown in Figs. 7(a) and 7(b). For the sake of clarity, we have separately shown the linear fitting for the data of Expt 2 in Figs. S5(a) and S5(b) (see Ref. [32]). The pressure coefficients and Grüneisen parameter are listed in Table II, and it can be observed that apparent changes in the pressure coefficient (a_1) of A_{1g} mode [2.4 and 1.7 cm^{-1} GPa^{-1} (Expt 1 and Expt 2)] between 0–1.8 and 1.8–4.0 GPa regions.

Generally, Raman linewidth is inversely proportional to the life time of the phonons for the crystalline materials. Hence, the linewidth of the Raman active phonon modes will give important information about the interactions existing in the solid system. For instance, electron-phonon, spin-phonon, and phonon-phonon coupling existing in the crystalline material and has been identified by Raman linewidth analysis [50–53]. So, to get the more detail about $TlBiS_2$, we have carefully analyzed the linewidth as a function of pressure and represented in Figs. 7(c) and 7(d). During the increase in pressure, systematic increase in the linewidth of the Raman peak is expected from quantum uncertainty principle. However, we had observed an unusual behavior in E_g mode. The full width at half maximum (FWHM) of the E_g peak decreases up to ∼1.8 GPa with the change in slope at ∼0.5 GPa. After that, the FWHM of the E_g peak increases with pressure up to

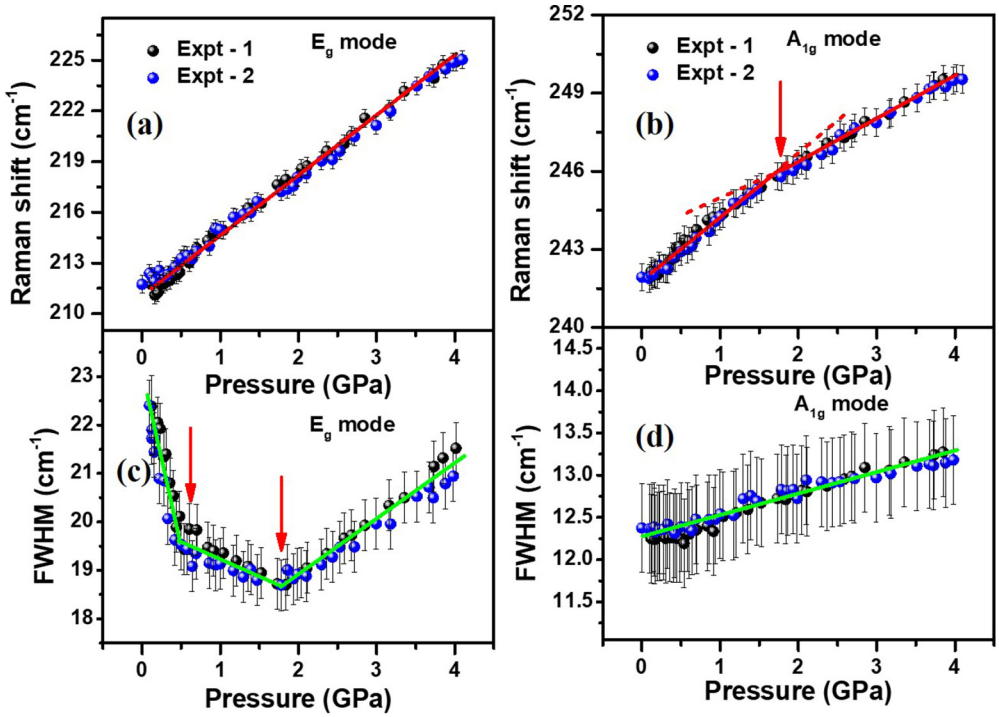

FIG. 7. Pressure dependence of the frequency of (a) E_g and (b) A_{1g} modes of $TlBiS_2$. (c) P vs FWHM of E_g mode and (d). P vs FWHM of A_{1g} mode. In (a)–(d), black (Expt-1) and blue (Expt-2) filled circles indicate data from two independent pressure runs. The error bars are obtained from instrumental error for these experiments. Solid red lines in (a) and (b) are linear fit to the first pressure run (Expt-1). Solid green lines in (c) and (d) are only guides to the eyes. Red arrows in (b) and (c) represent the isostructural electronic transitions. Red dashed line represents the extrapolation of the linear fit.

∼4.0 GPa. The FWHM of A_{1g} peak systematically increases with pressure up to ∼4.0 GPa. The changes in line width of the E_g mode at ∼0.5 GPa and ∼1.8 Pa is around ∼12.5% and ∼16.9%, respectively. Even though there are small changes in line width of the E_g mode from 0.5 GPa (around ∼19.6 cm^{-1}) to ∼1.8 GPa (around ∼18.6 cm^{-1}), but bigger than the one-pixel coverage of the spectrometer (instrumental error). Further, the trend in the FWHM has been reproducible over multiple experimental runs [see Figs. 7(c) and 7(d)] which also ascertains the observed inflection points. So, the clear observation of the two distinct inflection points at ∼0.5 and ∼1.8 GPa is an experimental fact. Further, the electron-phonon interaction can be understood from the electron-phonon coupling constant λ which is directly proportional to the Raman line width [21,54]. The calculated λ (see Fig. S6 in Ref. [32]) of E_g mode shows the systematic trend of the decreasing and then slight increasing nature which is matching well with the trend of an experimental line width of E_g mode. Therefore the changes in the Raman line width of E_g mode is attributed to electron-phonon coupling changes. Similar to our case, upon pressure, the decreasing line width of phonon modes has been observed during the topological transitions in black phosphorous and is attributed to the electron-phonon coupling changes with the help of

TABLE II. Experimental values of the Raman mode (E_g and A_{1g}) frequencies and its pressure coefficients at both ambient pressure and ∼1.80 GPa which is obtained from fits to the data using the linear equation $\omega(P) = \omega(P_0) + a_1(P - P_0)$. Here, $a_1 = (\frac{d\omega}{dP})$ represents the pressure coefficients (slope of the curve). The Grüneisen parameters γ are obtained by using the relation $\gamma = (\frac{B}{\omega(P0)} \times \frac{\partial\omega}{\partial P})$, where B represents the bulk modulus of $TlBiS_2$ ($B_0 = 37.65$ GPa).

Experimental run	Raman mode	Pressure Regions (GPa)	Mode frequency $\omega(P_0)$ (cm^{-1})	a_1 (cm^{-1} GPa^{-1})	Grüneisen Parameter γ
1	E_g	0–4.0	211.1 ± 0.1[a]	3.5 ± 0.1[a]	0.62
	A_{1g}	0–1.8	241.8 ± 0.1[a]	2.4 ± 0.1[a]	0.37
	A_{1g}	1.8–4.0	243.1 ± 0.1[b]	1.7 ± 0.0[b]	0.26
2	E_g	0–4.0	211.6 ± 0.1[a]	3.3 ± 0.0[a]	0.59
	A_{1g}	0–1.8	241.7 ± 0.1[a]	2.4 ± 0.1[a]	0.37
	A_{1g}	1.8–4.0	242.9 ± 0.1[b]	1.7 ± 0.1[b]	0.26

[a]Estimated at ambient pressure ($P_0 = 1$ atm).
[b]Estimated at $P_0 = 1.80$ GPa.

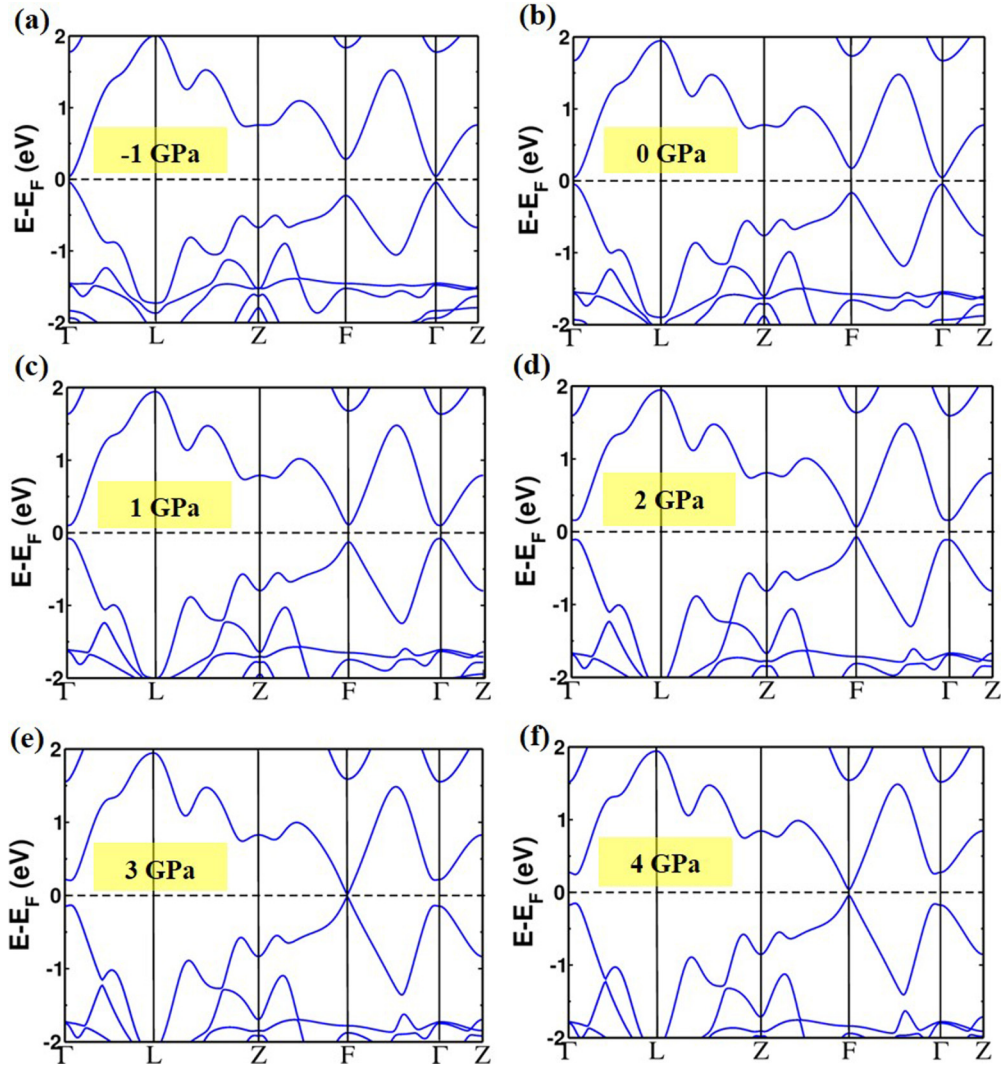

FIG. 8. (a)–(f) Electronic band structure of $TlBiS_2$ are calculated with SOC at different hydrostatic pressures (from −1 to 4 GPa). Band inversion takes place at the Γ and F points in the BZ as a function of pressure near $P_c^{\Gamma} = -0.4$ GPa and $P_c^{F} = 3.6$ GPa, respectively.

theoretical calculation of λ [21]. Since the $TlBiS_2$ shows the rhombohedral phase stability (as clearly observed in synchrotron XRD results) up to ∼4.0 GPa, the obtained linewidth anomalies cannot be due to the structural phase transition. So, the linewidth anomalies of A_{1g} and E_g mode at ∼0.5 and ∼1.8 GPa indicates the isostructural electronic transitions in $TlBiS_2$.

D. Theoretical calculations

To understand the experimentally observed Raman anomalies (isostructural transitions) at ∼0.5 and ∼1.8 GPa, we used first-principles calculations to simulate the rhombohedral phase (SG: $R\bar{3}m$) of $TlBiS_2$ as a function of pressure. Our estimates of the optimized lattice constants of $TlBiS_2$ are $a = 7.74$ Å and angle $\alpha = 31.03°$, which are within the typical GGA errors of experimental lattice parameters ($a = 7.67$ Å, $\alpha = 31.09°$). The calculated internal parameter characterizing the positions of the S atoms is $z = 0.261$. Electronic band structure of $TlBiS_2$ calculated including spin-orbit interaction at the optimized lattice constants reveals a direct band gap of 0.10 eV. Band gap estimated here is slightly lower than the experimental band gap of 0.42 eV, which is typical of DFT calculations of band gaps. The electronic structure of $TlBiS_2$ exhibits valleys at the Γ and F points of the BZ. The valence band maximum (VBM) at the Γ valley has higher energy than the VBM at the F valley [see Fig. 8(b)], whereas the conduction band minima (CBM) at the Γ valley is lower in energy than the CBM at the F valley. Band gaps estimated using optimized lattice constants (ambient pressure) at Γ and F points are 0.09 and 0.33 eV, respectively [see Fig. 8(b)]. It is noteworthy that Zhang *et al.* [18] estimated the band gap of 7 meV at 0 GPa (at Γ point). Further, in the electronic band structure of the $TlBiS_2$ system ($R\bar{3}m$ phase), the conduction bands are dominated by p orbitals of Bi and Tl and the valence bands are dominated by the p orbitals of S.

With increasing hydrostatic pressure, the CBM and VBM in both the valleys come closer and cross each other resulting in inversion of bands. A close examination of the electronic structure reveals that the critical pressures (P_c^{Γ} and P_c^{F})

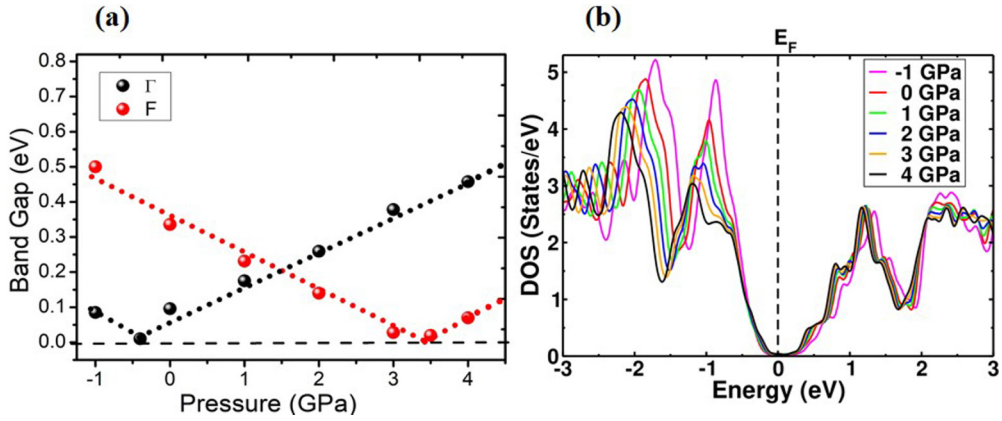

FIG. 9. (a) Evolution of band gap with hydrostatic pressure at Γ and F points showing the opening and closing of gaps at the critical pressures (P_C^{Γ} and P_C^{F}). (b) Electronic density of states of $TlBiS_2$ calculated with SOC at different hydrostatic pressures.

making band inversions at the Γ and F points are different. With increasing pressure from −1 to 4 GPa, the energy gap at the Γ point first closes and then reopens at close to $P \sim 0$ GPa, and similar behavior is found at F point with a critical pressure close to $P \sim 3$ GPa [see Fig. 9(a)]. These values of critical pressures (P_c^{Γ} and P_c^{F}) differ from previous calculations [18], primarily because of differences in estimated lattice constants due to different pseudopotentials, and exchange correlation functionals. Further, the pressure evolution of electronic density of states (DOS) is indicating that semiconducting nature of $TlBiS_2$ up to ∼4.0 GPa [see Fig. 9(b)]. At the Γ point, the band inversion occurs in between −0.5 and −0.3 GPa (i.e., $-0.5 < P_c^{\Gamma} < -0.3$ GPa, hence $P_c^{\Gamma} \sim -0.4$ GPa) and it is evident in the isosurfaces of charge densities [see Fig. 10(b)] associated with VBM and CBM at −0.3 and −0.5 GPa. On the other hand, the band gap separating the VBM and CBM at the F point is higher than the gap between them at the Γ point, hence higher pressure is required for the band inversion to occur at F point. Examining the isosurfaces of charge densities associated with VBM and CBM at the F

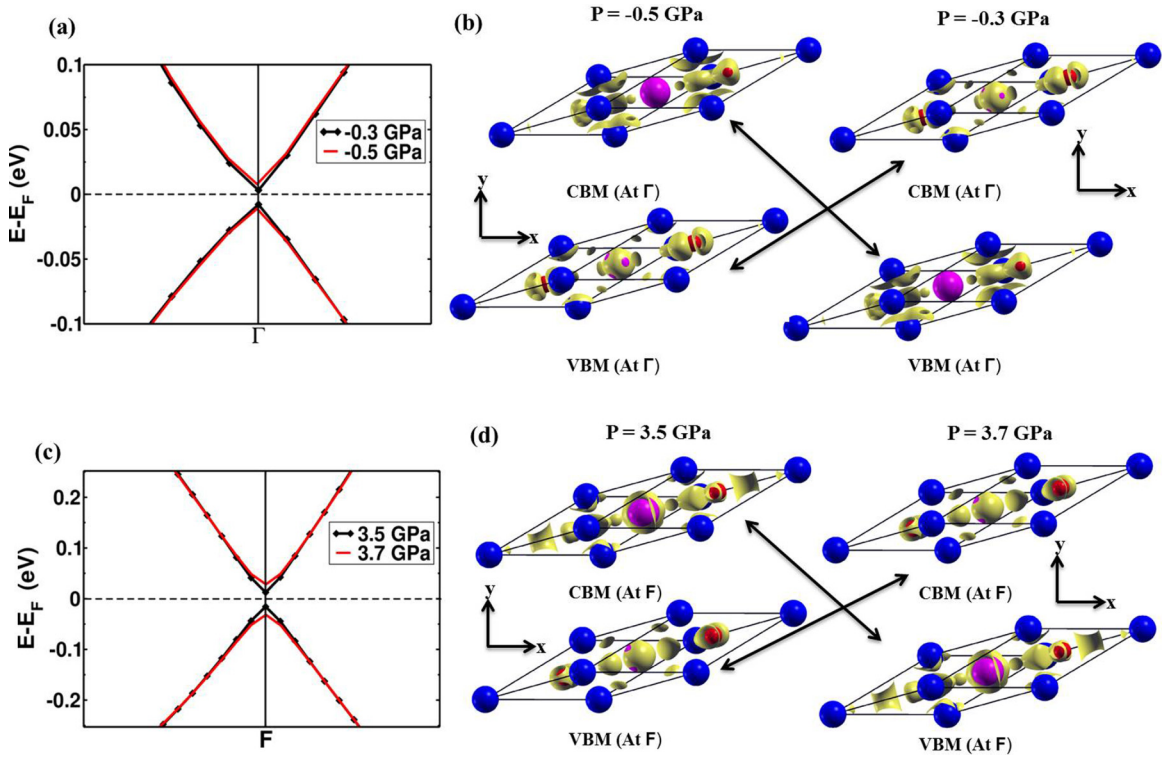

FIG. 10. Electronic structures of rhombohedral $TlBiS_2$ around the (a) Γ point and the (c) F point showing the band inversion between the top valence and lowest conduction bands as a function of hydrostatic pressures. (b) Isosurfaces of charge densities associated with VBM and CBM before and after the band inversion at the Γ point and the (d) F point reveal that the band inversion at Γ takes place in between −0.3 and −0.5 GPa (i.e., $-0.5 < P_c^{\Gamma} < -0.3$ GPa, hence $P_c^{\Gamma} \sim -0.4$ GPa at Γ point), whereas the band inversion at the F point occurs in between 3.5 and 3.7 GPa (i.e., $3.5 < P_c^{F} < 3.7$ GPa, $P_c^{F} \sim 3.6$ GPa at F point).

point [see Fig. 10(d)] at 3.5 and 3.7 GPa, it is clear that band inversion at the F point occurs in between 3.5 and 3.7 GPa (i.e., $3.5 < P_c^F < 3.7$ GPa, hence $P_c^F \sim 3.6$ GPa).

V. DISCUSSION

A TQPT is typically indicated by the crossing of valence and conduction bands at the critical pressures (P_c^Γ and P_c^F). To verify the change in topology due to band inversion, we determined the strong $\mathbb{Z}_2$ topological index using a robust, quantitative and exact method as employed in the Z2PACK code [43]. The strong $\mathbb{Z}_2$ topological invariant (υ_0) of $TlBiS_2$ calculated at -0.5 and -0.3 GPa is $\upsilon_0 = 0$ (normal insulator) and $\upsilon_0 = 1$ (TI), respectively. Thus $\mathbb{Z}_2$ topological index confirms the change in electronic topology and establishes the nontrivial band topology of $TlBiS_2$ at pressures greater than $P_c^\Gamma \sim -0.4$ GPa. We find that the topological invariants calculated at -1, 0, 1, 2, and 3 GPa ($\upsilon_0 = 0$, 1, 1, 1, and 1 respectively), are consistent with the band inversion picture. To probe the effect of second band inversion which occurs at F point on the electronic topology we examined the $\mathbb{Z}_2$ topological invariant at 3.5 and 3.7 GPa. $TlBiS_2$ changes from a strong TI at 3.5 GPa ($\upsilon_0 = 1$) to a system with trivial topology at 3.7 GPa ($\upsilon_0 = 0$). Thus the $\mathbb{Z}_2$ topological index-based argument confirms a trivial phase resulting from even number of band inversions at the TRIM points (above 3.6 GPa). Besides, the importance of SOC for this class of materials was systematically studied and analyzed in our calculations by performing electronic structure calculations using scalar relativistic potentials as well (please see Fig. S7) and results are discussed in Ref. [32].

The even number of band inversions is an indicator of the TCI phase. In our system, the band gap closes and reopens with an even number of inversions between the two extreme pressures (-0.4 and 3.6 GPa). This implies that even though the phase above 3.6 GPa cannot be a $\mathbb{Z}_2$ TI, we obtain a TCI phase driven by the mirror symmetry of the hexagonal lattice. Hence we have calculated the mirror Chern number (n_M) as a function of pressure. The mirror Chern number (n_M) of $TlBiS_2$ calculated at 3.5 GPa and 3.7 GPa is $n_M = 1$ and $n_M = 2$ (TCI), respectively. Thus n_M confirms the change in electronic topology and establishes the non-trivial band topology of $TlBiS_2$ with respect to TCI phase characterized by $n_M = 2$ at pressures greater than 3.6 GPa. In summary, ongoing from -0.5 to -0.3 GPa the odd number of inversions occurring at Γ point results in a change of $\mathbb{Z}_2$ topological invariant from 0 to 1. At pressures greater than 3.6 GPa, i.e., following the second band inversion a total even number of inversions (3 from F and 1 from Γ) results in $n_M = 2$ and $\mathbb{Z}_2$ topological index 0. The comparison between invariant quantities $\mathbb{Z}_2$ and n_M are shown in the Table III.

The experimentally observed Raman signatures of multiple isostructural electronic transitions are closely consistent with our DFT theoretical prediction. Therefore we attribute the linewidth anomalies of E_g mode at $\sim$0.5 GPa to the nontrivial TQPT which is a consequence of band inversion at Γ of the BZ. Similarly, the phonon anomalies at $\sim$1.8 GPa can be attributed to TCI phase as a consequence of even number of band inversion (three from F and one from Γ) of the BZ. In both the band inversions (Γ and A points), VBM characters (dominated by S p orbitals) are exchanged with CBM characters (dominated by p orbitals of Bi and Tl). During the exchange of the orbital characters, the charge gets redistributed between VBM and CBM which further modulates the electronic structure. Consequently, here Raman active phonon (E_g) life time is getting affected, which reflect the unusual electron-phonon coupling at $\sim$0.5 and $\sim$1.8 GPa in Raman linewidth. Note that there is a small difference between the experimental (0.5 and 1.8 GPa) and theoretical critical pressure values (-0.4 and 3.6 GPa). This difference in the critical pressure values can arise from the various factors such as temperature, the typical error in calculated lattice parameters and band gaps (depends on the pseudo potential and exchange correlation functional), etc. In fact, many high-pressure experiments present the mismatches of the critical pressure values with first-principles theoretical calculations [24,51] that could mainly originate from various approximations used in the theoretical approach. For example, theoretical calculations predict the transition pressure of band inversions at L and A point of the BZ in 1T-$TiTe_2$ at $\sim$0.88 and $\sim$3.40 GPa, however experimentally phonon anomalies are noticed at $\sim$2.0 and $\sim$4.0 GPa respectively [24]. Similarly, in BiTeI, the topological phase transition points (as a consequence band inversion at A points) are calculated to be 1.7 and 4.1 GPa corresponding to the calculation based on local density approximations (LDA) and GGA respectively [8]. However, experimentally observed transition point is $\sim 2.0 - 2.9$ GPa [9]. These two above examples demonstrate the commonly observed mismatch between the high-pressure experimental and theoretical transition pressure values. However, we have clearly seen two isostructural electronic transitions through Raman phonon anomalies at $\sim$0.5 and $\sim$1.8 GPa within the stability range of the rhombohedral symmetry of $TlBiS_2$ compound and the transition pressure values qualitatively agree with the DFT based theoretical predictions (-0.4 and 3.6 GPa). Further, the comparison of the critical transition pressure value between our theory and literature [18] is discussed in Ref. [32].

Even though the nontrivial topological phase of $TlBiS_2$ was predicted at 0 GPa (ambient condition), ARPES measurements reveal that $TlBiS_2$ is a direct band gap semiconductor ($E_g = 0.42$ eV) and is topologically trivial ($\mathbb{Z}_2 = 0$) at ambient condition [20]. The obvious reason for this contradiction is the under estimation of the band gap using GGA. So, the direct observation (using ARPES) [20] of the band gap ($E_g = 0.42$ eV) clearly suggesting that first band inversion has to occur at above 0 GPa and consistent with our experimental results. Therefore the applied pressure increases the effective

TABLE III. Mirror Chern number (n_M) and $\mathbb{Z}_2$ topological index of $TlBiS_2$ calculated at 3.5 GPa and 3.7 GPa. The second band inversion at F around $P_\Gamma^C \sim 3.6$ GPa results in a TCI phase characterized by $n_M = 2$ and $\upsilon_0 = 0$ (trivial with respect to $\mathbb{Z}_2$ TIs).

Pressure (GPa)	$\mathbb{Z}_2$ Topological index	Mirror Chern number (n_M)
3.5	1	1
3.6	0	2

strength of the SOC, decreases band gap and at a critical pressure point (∼0.5 GPa) a phase transition takes place from topologically trivial to nontrivial state as a consequence of the first band inversion at the Γ point. Further, the evolution of electronic structure with hydrostatic pressure corroborates that $TlBiS_2$ which remains a direct band gap semiconductor up to 4 GPa with bulk calculated band gaps of 0.10, 0.17, 0.14, 0.03, 0.07, and 0.19 eV for pressures of 0, 1, 2, 3, and 4 GPa, respectively. At pressure (P) ∼2 GPa, we observe a shift in the CBM and VBM at the Γ to those at the F point. With increasing hydrostatic pressure, the Fermi level [marked with the dashed horizontal black line in Figs. 8(a) to 8(f)] does not cross the top valence band and bottom conduction band is indicating that $TlBiS_2$ does not undergo a semiconductor to metal phase transition. Further, the pressure dependence of the theoretically calculated phonon modes (A_{1g} and E_g) are commented in Ref. [32].

The pressure dependent electronic band structure (calculated) of $TlBiS_2$ reveals that there is no overlap near the Fermi energy across any other directions of the BZ, except two successive band inversions at Γ and F point. This feature might be very interesting because the electronic contribution from the band inversions (only) can be understood in detail by transport measurements. It is noteworthy that, four consecutive bands inversions are predicted in 1T-$TiTe_2$ under hydrostatic pressure [29], and experimentally two band inversions are claimed by phonon and electrical transport anomalies [24]. However, in 1T-$TiTe_2$, the electronic bands are crossing over other direction of the BZ (in addition to band inversion points) near the Fermi energy which makes the system quite difficult to deal with transport tools for only studying the topological contributions. So, here the successive band inversions and clean band structure (under pressure evolution) make the $TlBiS_2$ system unique and it is material specific. Hence, the $TlBiS_2$ compound could be an ideal candidate for exploring much exciting physics behind topology, and its effect in multiple properties. The two iso-structural electronic transitions at ∼0.5 and ∼1.80 GPa demonstrated by the occurrence of the unusual electron-phonon coupling by both the experiment and the first principles theoretical calculations, can be attributed to nontrivial TQPT and TCI transition respectively. Further, the larger atomic mass (Tl and Bi), the narrow band gap semiconducting nature of $TlBiS_2$ compound (up to ∼4.0 GPa) and multiple band inversions (topological phase transitions) can be expected to give the good thermoelectric performance under pressure. Besides, the existence of topological states ($\mathbb{Z}_2 = 1$) in $TlBiS_2$ at relatively low pressure regions from 0.5 GPa to 1.8 GPa (experimentally accessible pressure regions), hence this system may be useful for next generation spintronic and thermoelectric devices operating in the mechanically strained environment. Finally, we hope our interesting results will stimulate research interest on $TlBiS_2$, particularly for Shubnikov de Haas oscillation measurement under pressure [31] which may provide further insight into observed TQPT.

VI. CONCLUSION

In summary, a combination of high-pressure Raman scattering and synchrotron diffraction measurements confirms that $TlBiS_2$ undergoes a first-order structural phase transition at ∼4.0 GPa. Furthermore, the E_g phonon linewidth anomalies at ∼0.5 and ∼1.8 GPa are observed due to unusual electron-phonon coupling in the rhombohedral phase of $TlBiS_2$. We have attributed the two isostructural electronic transitions at ∼0.5 and ∼1.80 GPa, respectively, to the nontrivial TQPT ($\mathbb{Z}_2 = 1$) and TCI ($n_M = 2$) transitions based on our first-principles theoretical calculations. We are sure that our results will motivate further research interest in $TlBiS_2$ on the aspect of quantum oscillations measurements under pressure.

ACKNOWLEDGMENTS

Authors V.R., R.A., and S.C.S. sincerely thank JNCASR for the research fellowship. The authors gratefully acknowledge the Department of Science and Technology (DST) for the financial support to carry out the high-pressure synchrotron XRD measurements at the Xpress beam line, Elettra synchrotron, Trieste, Italy. B.J. acknowledges IISc Bangalore and ICTP Trieste for support through an IISc-ICTP fellowship. Also, S.C.P. and C.N. thank DST-SERB for the financial support under Grant No. SB/S2/CMP-019/2014. UVW is grateful to the DST for support through a JC Bose national fellowship.

[1] M. Z. Hasan and C. L. Kane, Rev. Mod. Phys. **82**, 3045 (2010).
[2] B. A. Bernevig, T. L. Hughes, and S.C. Zhang, Science **314**, 1757 (2006).
[3] M. König, S. Wiedmann, C. Brüne, A. Roth, H. Buhmann, L. W. Molenkamp, X.-L. Qi, and S.-C. Zhang, Science **318**, 766 (2007).
[4] H. Zhang, C.X. Liu, X.-L. Qi, X. Dai, Z. Fang, and S.C. Zhang, Nat. Phys. **5**, 438 (2009).
[5] Y. Xia, D. Qian, D. Hsieh, L. Wray, A. Pal, H. Lin, A. Bansil, D. Grauer, Y. S. Hor, R. J. Cava, and M. Z. Hasan, Nat. Phys. **5**, 398 (2009).
[6] Y. L. Chen, J. G. Analytis, J. H. Chu, Z. K. Liu, S. K. Mo, X. L. Qi, H. J. Zhang, D. H. Lu, X. Dai, Z. Fang, S. C. Zhang, I. R. Fisher, Z. Hussain, and Z. X. Shen, Science **325**, 178 (2009).
[7] D. Hsieh, Y. Xia, D. Qian, L. Wray, F. Meier, J. H. Dil, J. Osterwalder, L. Patthey, A. V. Fedorov, H. Lin, A. Bansil, D. Grauer, Y. S. Hor, R. J. Cava, and M. Z. Hasan, Phys. Rev. Lett. **103**, 146401 (2009).
[8] M. S. Bahramy, B. J. Yang, R. Arita, and N. Nagaosa, Nat. Commun. **3**, 679 (2012).
[9] X. Xi, C. Ma, Z. Liu, Z. Chen, W. Ku, H. Berger, C. Martin, D. B. Tanner, and G. L. Carr, Phys. Rev. Lett. **111**, 155701 (2013).
[10] L. Fu, C. L. Kane, and E. J. Mele, Phys. Rev. Lett. **98**, 106803 (2007).
[11] J. C. Y. Teo, L. Fu, and C. L. Kane, Phys. Rev. B **78**, 045426 (2008).
[12] L. Fu, Phys. Rev. Lett. **106**, 106802 (2011).

[13] Y. Tanaka, Z. Ren, T. Sato, K. Nakayama, S. Souma, T. Takahashi, K. Segawa, and Y. Ando, Nat. Phys **8**, 800 (2012).
[14] T. H. Hsieh, H. Lin, J. Liu, W. Duan, A. Bansil, and L. Fu, Nat. Commun. **3**, 982 (2012).
[15] W. Liu, X. Peng, C. Tang, L. Sun, K. Zhang, and J. Zhong, Phys. Rev. B **84**, 245105 (2011).
[16] A. Bera, K. Pal, D. V. S. Muthu, S. Sen, P. Guptasarma, U. V. Waghmare, and A. K. Sood, Phys. Rev. Lett. **110**, 107401 (2013).
[17] Y. L. Chen, Z. K. Liu, J. G. Analytis, J. H. Chu, H. J. Zhang, B. H. Yan, S. K. Mo, R. G. Moore, D. H. Lu, I. R. Fisher, S. C. Zhang, Z. Hussain, and Z. X. Shen, Phys. Rev. Lett. **105**, 266401 (2010).
[18] Q. Zhang, Y. Cheng, and U. Schwingenschlögl, Sci. Rep. **5**, 8379 (2015).
[19] R. J. Cava, H. Ji, M. K. Fuccillo, Q. D. Gibson, and Y. S. Hor, J. Mater. Chem. C **1**, 3176 (2013).
[20] T. Sato, K. Segawa, K. Kosaka, S. Souma, K. Nakayama, K. Eto, T. Minami, Y. Ando, and T. Takahashi, Nat. Phys. **7**, 840 (2011).
[21] S. N. Gupta, A. Singh, K. Pal, B. Chakraborti, D. V. S. Muthu, U. V. Waghmare, and A. K. Sood, Phys. Rev. B **96**, 094104 (2017).
[22] Y. S. Ponosov, T. V. Kuznetsova, O. E. Tereshchenko, K. A. Kokh, and E. V. Chulkov, JETP Lett. **98**, 557 (2014).
[23] P. P. Kong, F. Sun, L. Y. Xing, J. Zhu, S. J. Zhang, W. M. Li, Q. Q. Liu, X. C. Wang, S. M. Feng, X. H. Yu, J. L. Zhu, R. C. Yu, W. G. Yang, G. Y. Shen, Y. S. Zhao, R. Ahuja, H. K. Mao, and C. Q. Jin, Sci. Rep. **4**, 6679 (2014).
[24] V. Rajaji, U. Dutta, P. C. Sreeparvathy, S. C. Sarma, Y. A. Sorb, B. Joseph, S. Sahoo, S. C. Peter, V. Kanchana, and C. Narayana, Phys. Rev. B **97**, 085107 (2018).
[25] V. Rajaji, S. Janaky, S. C. Sarma, S. C. Peter, and C. Narayana, J. Phys.: Condens. Matter **31**, 165401 (2019).
[26] V. Rajaji, K. Pal, S. C. Sarma, B. Joseph, S. C. Peter, U. V. Waghmare, and C. Narayana, Phys. Rev. B **97**, 155158 (2018).
[27] K. Saha, K. Légaré, and I. Garate, Phys. Rev. Lett. **115**, 176405 (2015).
[28] W. Li, X. Y. Wei, J. X. Zhu, C. S. Ting, and Y. Chen, Phys. Rev. B **89**, 035101 (2014).
[29] Q. Zhang, Y. Cheng, and U. Schwingenschlögl, Phys. Rev. B **88**, 155317 (2013).
[30] Z. Zhu, Y. Cheng, and U. Schwingenschlögl, Sci. Rep. **4**, 4025 (2014).
[31] J. Park, K. H. Jin, Y. J. Jo, E. S. Choi, W. Kang, E. Kampert, J. S. Rhyee, S. H. Jhi, and J. S. Kim, Sci. Rep. **5**, 15973 (2015).
[32] See Supplemental Material at http://link.aps.org/supplemental/10.1103/PhysRevB.99.184109 for additional experimental (synthesis, Raman, and synchrotron XRD analysis) and theoretical results.
[33] J. C. Chervin, B. Canny, and M. Mancinelli, High pressure Res. **21**, 305 (2001).
[34] S. Klotz, J. C. Chervin, P. Munsch, and G. L. Marchand, J. Phys. D: Appl. Phys. **42**, 075413 (2009).
[35] A. P. Hammersley, S. O. Svensson, M. Hanfland, A. N. Fitch, and D. Hausermann, High Pressure Res. **14**, 235 (1996).
[36] J. Rodríguez-Carvajal, Physica B **192**, 55 (1993).
[37] QUANTUMESPRESSO is a community project for high-quality quantum-simulation software, based on density-functional theory, and coordinated by P. Giannozzi. See http://www.quantum-espresso.org and http://www.pwscf.org.
[38] X. Hua, X. Chen, and W. A. Goddard, Phys. Rev. B **55**, 16103 (1997).
[39] J. P. Perdew, K. Burke, and M. Ernzerhof, Phys. Rev. Lett. **77**, 3865 (1996).
[40] G. Kresse and D. Joubert, Phys. Rev. B **59**, 1758 (1999).
[41] A. Dal Corso, Comput. Mat. Sci. **95**, 337 (2014).
[42] S. Baroni, S. de Gironcoli, A. Dal Corso, and P. Giannozzi, Rev. Mod. Phys. **73**, 515 (2001).
[43] D. Gresch, G. Autès, O. V. Yazyev, M. Troyer, D. Vanderbilt, B. A. Bernevig, and A. A. Soluyanov, Phys. Rev. B **95**, 075146 (2017).
[44] A. A. Soluyanov and D. Vanderbilt, Phys. Rev. B **83**, 235401 (2011).
[45] J. Bhattacharjee and U. V. Waghmare, Phys. Rev. B **71**, 045106 (2005).
[46] C. L. Teske and W. Bensch, Acta Cryst. E **62**, i163 (2006).
[47] F. D. Murnaghan, Proc. Nat. Acad. Sci. USA **30**, 244 (1944).
[48] R. Vilaplana, D. Santamaría-Pérez, O. Gomis, F. J. Manjón, J. González, A. Segura, A. Muñoz, P. Rodríguez-Hernández, E. Pérez-González, V. Marín-Borrás, V. Muñoz-Sanjose, C. Drasar, and V. Kucek, Phys. Rev. B **84**, 184110 (2011).
[49] M. Yanmei, L. Guangtao, Z. Pinwen, W. Hui, W. Xin, C. Qiliang, L. Jing, and M. Yanming, J. Phys.: Condens. Matter **24**, 475403 (2012).
[50] M. Cardona, High Pressure Res. **24**, 17 (2004).
[51] V. Rajaji, P. S. Malavi, S. S. R. K. C. Yamijala, Y. A. Sorb, U. Dutta, S. N. Guin, B. Joseph, S. K. Pati, S. Karmakar, K. Biswas, and C. Narayana, Appl. Phys. Lett. **109**, 171903 (2016).
[52] R. S. Joshya, V. Rajaji, C. Narayana, A. Mascarenhas, and R. N. Kini, J. Appl. Phys. **119**, 205706 (2016).
[53] Y. A. Sorb, V. Rajaji, P. S. Malavi, U. Subbarao, P. Halappa, S. C. Peter, S. Karmakar, and C. Narayana, J. Phys.: Condens. Matter **28**, 015602 (2016).
[54] M. Lazzeri, S. Piscanec, F. Mauri, A. C. Ferrari, and J. Robertson, Phys. Rev. B **73**, 155426 (2006).